aerospace

MDPI

Article

Investigation of a Portable Wind Tunnel for Energy Harvesting

Haigang Tian [1], Tianyi Hao [2,*], Chao Liu [3], Han Cao [1] and Xiaobiao Shan [1,*]

[1] State Key Laboratory of Robotics and System, Harbin Institute of Technology, Harbin 150001, China; 18b908022@stu.hit.edu.cn (H.T.); ershugm@gmail.com (H.C.)
[2] Chinese Flight Test Establishment, Xi'an 710089, China
[3] Xi'an Military Representative Bureau of Army Armament Department, Xi'an 710089, China; liuchao2020xa@163.com
* Correspondence: haotianyi2@163.com (T.H.); shanxiaobiao@hit.edu.cn (X.S.)

Abstract: Current wind tunnels possess a large space volume and high manufacturing cost, which are not suitable for investigating micro energy harvesters. This paper aims to design and fabricate a small, portable and low-speed wind tunnel for energy harvesting. A wind tunnel structure was first designed, a finite element analyses is then utilized to obtain the airflow velocity and turbulence intensity at the testing section, and the influence of the structural parameters of the wind tunnel on the flow field performance is finally investigated to achieve better performance. An experimental prototype of the wind tunnel was fabricated to verify the simulation results. Results demonstrated that the distribution uniformity and average turbulence intensity at the test section decrease first and then increase with the increase of both the diffuser and contraction lengths. The rectifying and damping effect of the honeycomb increase with increasing porosity and thickness. When the diffuser and contraction lengths are 850 mm and 480 mm, respectively, a better distribution uniformity and a lower turbulence intensity can be achieved. Experimental results were in good agreement with the simulation values. The maximum airflow velocity can reach up to 24.74 m/s, and the minimum error was only 1.23%. The designed wind tunnel achieved low-speed, small, portable and stable functions. This work provides an important guidance for further investigating the piezoelectric energy harvesting.

Keywords: wind tunnel; simulation analyses; flow field performance; optimization design; experimental validation; energy harvesting

Citation: Tian, H.; Hao, T.; Liu, C.; Cao, H.; Shan, X. Investigation of a Portable Wind Tunnel for Energy Harvesting. *Aerospace* **2021**, *8*, 386. https://doi.org/10.3390/aerospace8120386

Academic Editor: Bosko Rasuo

Received: 2 September 2021
Accepted: 4 December 2021
Published: 9 December 2021

1. Introduction

Wind tunnels are considered an important research tool for designing and evaluating aerospace vehicles [1,2], wind energy harvesters [3], bridges [4,5], automobiles [6], and buildings [7–9]. The current experimental investigations for energy harvesting are mainly conducted in larger volume wind tunnels. However, to investigate the aeroelastic vibration response and harvesting characteristics of small airfoil-based energy harvester, the utilization of a large wind tunnel poses some problems, such as high manufacturing cost and larger space volume [10,11]. Therefore, it is necessary to design and fabricate a small, portable and low-speed wind tunnel experimental system to investigate the aeroelastic dynamics response of small airfoil-based aircrafts.

The major components of a wind tunnel include the diffuser, rectification (honeycomb and screens), contraction, and test section. The diffuser section plays an essential role in connecting the blower and rectification section. The kinetic energy output by the blower is converted into airflow pressure, so that the airflow velocity is fully slowed down through the change of cross-section of the diffuser section [12]. The rectification section aims to stabilize the airflow by means of the honeycomb and screens. The main function of the contraction section is to increase the average velocity. In principle, the problem of contraction design is a search for the optimum shape with minimum nozzle length for

a desirable flow quality at the end of the nozzle [13]. The contraction curves commonly include the Vitoshinsky, bicubic, fifth power curve, and multi-axis Vitoshinsky. Mehta et al. [14] proposed a set of design principles for small and low-velocity open-loop wind tunnels and summarized some guiding principles for structural parameters design. Goran et al. [15] performed a measurement and an assessment of flow quality in the T-35 wind tunnel, which demonstrated that the variation of a total pressure in the test section was below 0.1%. Rasuo [16–18] analyzed the accuracy influence factors of two-dimensional wind tunnel, and the obtained factors were able to contribute to the increased accuracy of the measured aerodynamic values.

Computational fluid dynamics (CFD) has been widely used in wind tunnel design [19,20]. It is a valuable tool for measuring the flow fields and evaluating the spatial variation that often cannot be sufficiently obtained by experimental measurements [21,22]. It can also be used to meet specific analytical requirements, such as wind tunnel acoustic analyses [23–28]. Calautit et al. [29] adopted numerical investigations into the design and simulation of the flow parameters in a closed-loop subsonic wind tunnel, which demonstrated that adding the guide vanes to the wind tunnel upstream corners improved the airflow uniformity by 36% and combining the upstream with downstream guide vanes improved the uniformity by 65%. Leifsson et al. [30] used a high-fidelity CFD flow solver to capture the nonlinear flow field. Due to the high computational expense of the CFD simulation, surrogate-based optimization (SBO) was used to accelerate the design process and obtained better performance.

As can be seen from the above review, the larger volume and high-cost wind tunnels for investigating larger spacecraft systems have been well explored. However, to the best of the authors knowledge, the larger volume wind tunnels were not suitable for investigating micro energy harvesters. In addition, a small, portable and low-speed wind tunnel has not been documented in the open literature to date. There is a need to investigate a small and portable wind tunnel for micro piezoelectric energy harvester.

Therefore, this paper presents the design of a small, portable and low-speed open-loop wind tunnel. The structure of this paper is as follows: the working principle of the wind tunnel is demonstrated in Section 2; the effects of both diffuser and contraction lengths as well as honeycomb parameters on wind velocity uniformity and turbulence intensity are investigated in Section 3; the experimental prototype of the wind tunnel is fabricated, the experimental analyses are conducted, and the obtained simulation results based on CFD are validated against the experimental values in Section 4; the conclusions of this work are drawn in Section 5.

2. Structure and Working Principle of Wind Tunnels

The small wind tunnel designed in this paper adopts the direct flow structure, that is, airflow from the blower directly enters the environment after passing through the diffuser, rectification, contraction, and test section. Compared with a closed-loop wind tunnel, it possesses the advantages of having a small floor space and low cost. The designed wind tunnel structure is illustrated in Figure 1.

The wind tunnel consists of the diffuser, rectification, contraction, and test section, which is supported by stands. The fan blows rather than sucks the airflow in the designed wind tunnel. The diffuser plays the role of connecting the blower and the rectification section. The rectification section is the key component in the open-loop wind tunnel. The flow vortex can be divided and straightened by installing the honeycomb and screens at the rectification section, and the radial velocity component is attenuated. The main function of the contraction section is to increase the average velocity and ensure that the wind velocity in the test section meets the designed requirements. The contraction section can also decrease the velocity fluctuation to a fraction of the original. The test section of the wind tunnel is the working section where the piezoelectric energy harvester is installed and aerodynamic tests are performed. The cross section of the designed test section was

300 mm × 300 mm. It was designed to adequately guarantee a stable and uniform airflow at the test section.

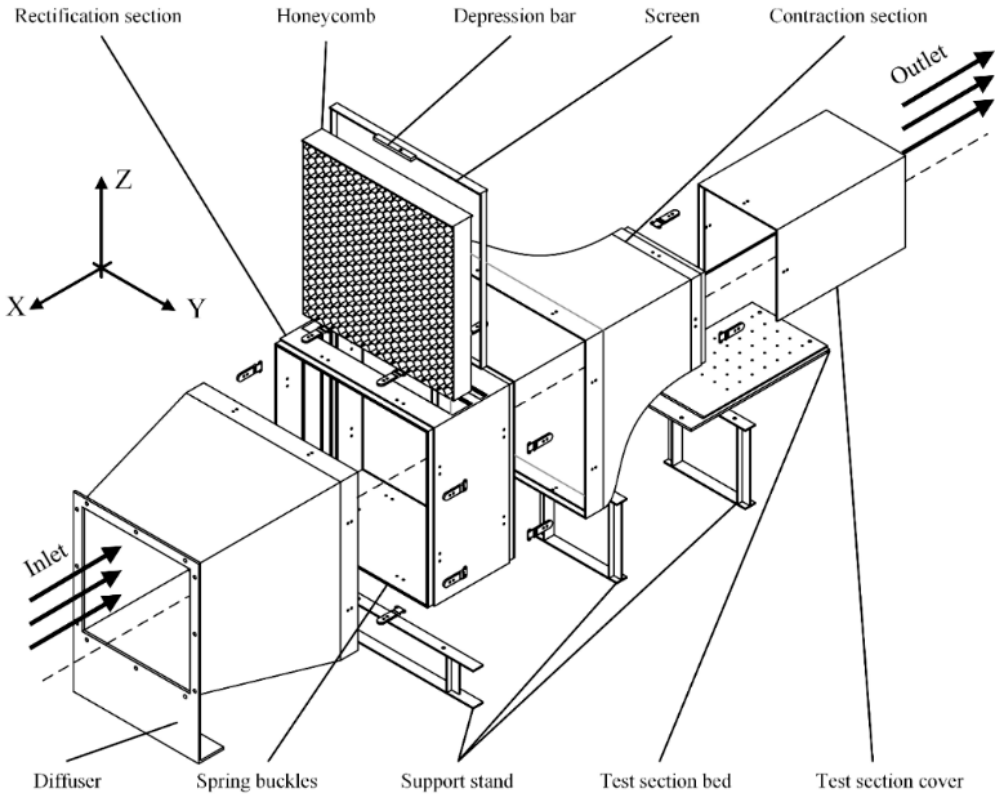

Figure 1. Structural diagram of the designed wind tunnel.

The wind tunnel was fabricated by using transparent acrylic material, which was convenient to observe the tested system in the test section. The wind tunnel adopts a modular design, the rubber gasket between each section ensures the air tightness, the spring buckles aim to lock, and the grooves guarantee the assembly accuracy. When not in use, it could be taken apart and folded to reduce the floor space. Therefore, the designed wind tunnel possesses the small and portable advantages.

3. Optimization Designing of the Structural Parameters

The flow field quality of the open-loop wind tunnel is mainly affected by the diffuser length, contraction length, and honeycomb. The optimized structural parameters of wind tunnel can be obtained by using CFD methods. The diffuser section slowly expands and recovers the kinetic energy into pressure energy, which helps to stabilize the pressure and reduces the influence of turbulence in the working environment. Generally, the diffuser angle of the large-angle diffuser ranges from 5° to 8° and does not exceed 25°.

The contraction section aims to produce a stable and uniform airflow at its outlet and avoid boundary layer separation. Three important parameters that determine the performance of the contraction section are contraction ratio, contraction curve, and length. The contraction ratio C is defined as the ratio of the inlet section area to the outlet. If the contraction ratio is very small, it cannot fully accelerate the airflow and reduce the velocity fluctuation. On the contrary, it requires increasing the cross-sectional area of the rectification section, and thus leads to increasing the overall size of the wind tunnel. Considering the length of the wind tunnel and the connection with the rectification section, C was defined as 4 in this paper, that is, the cross area of the outlet section was 300 mm × 300 mm, and the inlet section was 600 mm × 600 mm.

When designing the contraction section, a shape curve that simultaneously reduces overall wind tunnel losses and provides a high-quality airflow at the test section was first

selected [31]. Several common contraction curves include the Vitoshinsky curve, bicubic curve, fifth curve and multi-axis Vitoshinsky curve. The steep rate of the Vitoshinsky curve gradually decreases along the axial direction, which is beneficial to stabilize the airflow at the outlet of the contraction section. Therefore, the Vitoshinsky curve was selected for designing the wind tunnel, which is written as follows:

$$R = \frac{R_2}{\sqrt{1 - \left[1 - \left(\frac{R_2}{R_1}\right)^2\right] \frac{\left(1 - \frac{x^2}{L^2}\right)^2}{\left(1 + \frac{x^2}{3L^2}\right)^3}}} \quad (1)$$

where, R_1 represents the inlet radius of the contraction section; R_2 is the outlet radius; R represents the section radius at the axial distance of x; L refers to the length of the contraction section.

Figure 2 illustrates the Vitoshinsky curve diagram.

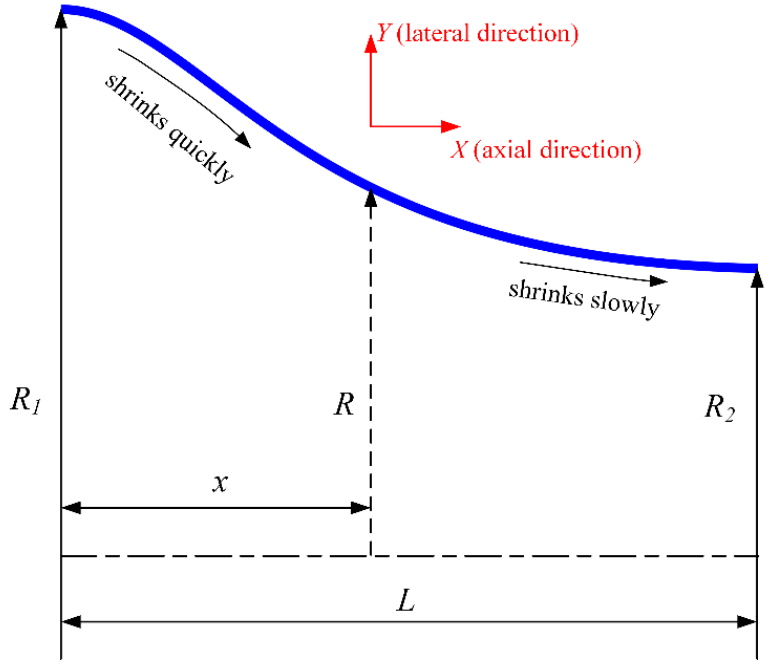

Figure 2. Vitoshinsky curve.

The influence of the diffuser angle and length of the contraction section on the flow field uniformity at the test section was fully investigated by using CFD methods. The structural parameters of the wind tunnel were first designed, the finite element model of the wind tunnel was then established, and the simulation analyses were conducted to obtain the numerical data. The realizable *k*–epsilon turbulence model was adopted, which is capable of obtaining a highly accurate prediction of the flow field. The mass flow rate was set as 7800 m^3/s in the simulation analyses, which was equal to that of the blower. Therefore, the obtained airflow velocity ranged from 19 m/s to 28 m/s at the test section. The diffuser and contraction lengths were selected as the variables, and thus the obtained diffuser angle was decimal. The selected structural parameters of diffuser and contraction section are shown in Table 1.

Table 1. Lengths of diffuser and contraction section.

Diffuser length (mm)	650	700	750	800	850	900	950	1000	1050
Diffuser angle (°)	9.74	9.04	8.43	7.90	7.44	7.02	6.65	6.32	6.01
Contraction length (mm)	320	360	400	440	480	520	560	600	640

3.1. Influence of Diffuser Length on Flow Field Uniformity

The diffuser section of the wind tunnel connects the blower and the rectification section. The kinetic energy output by the blower is transformed into pressure energy by changing the cross-sectional area, so that the airflow is sufficiently slowed down. It is convenient for the honeycomb and screens to be placed at the rectification section to stabilize the airflow and reduce the energy loss. The smaller the diffuser angle is, the less prone to boundary layer separation and the better the flow quality can be obtained. However, the smaller diffuser angle could lead to the longer length of the diffuser. In order to obtain the optimal length of the diffuser, the flow field characteristics of the test section under different diffuser lengths were investigated. Figure 3 illustrates the axial wind velocity distribution along the centerline of the test section under different diffuser lengths. Therein, the centerline ranges from the inlet (x = 0 m) to the outlet (x = 0.55 m). Therein, the length refers to the required length that stabilizes the flow in Figure 3; the origin of the x-axis represents the connection location between the contraction and test sections.

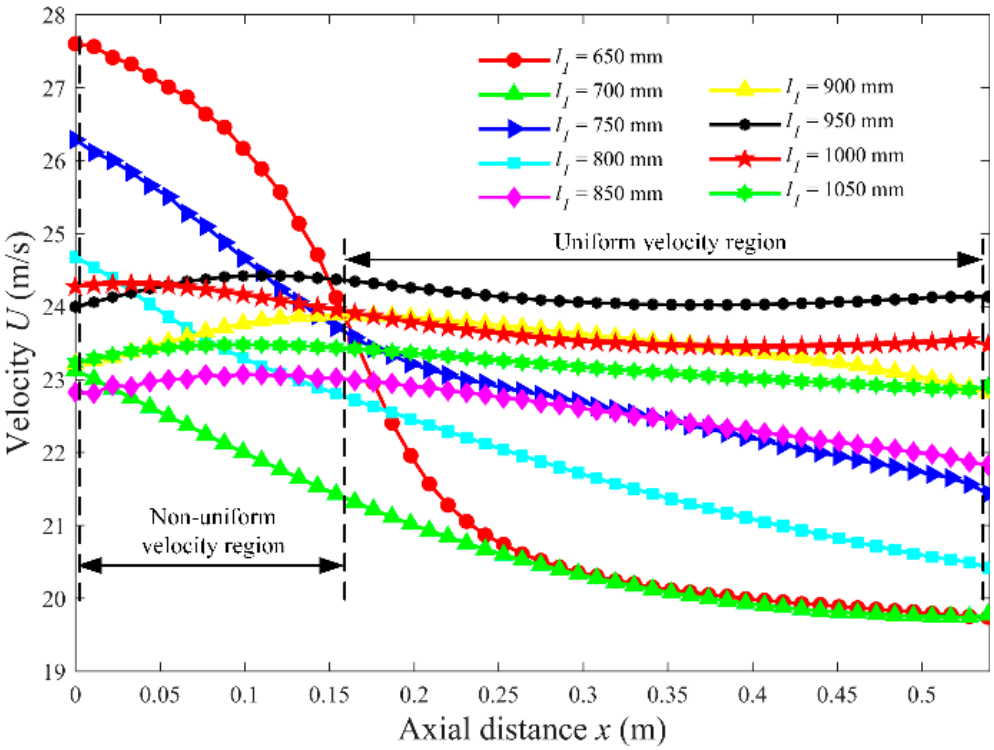

Figure 3. Velocity distribution characteristics at different diffuser lengths.

As can be seen in Figure 3, the uniformity of the velocity distribution of the testing section is improved with the increase of the length of the diffuser section. When the diffuser length is up to 850 mm, the velocity distribution reaches a relatively uniform effect. When increasing the length further, the uniformity of the wind velocity at the test section does

not increase significantly. Therefore, a diffuser length of 850 mm can achieve better velocity uniform distribution. It is recommended to adopt a diffuser length of 850 mm in designing the wind tunnel.

To clearly demonstrate the flow field characteristics of the wind tunnel, Figure 4 illustrates the velocity contour under different diffuser lengths. Therein, the contour represents the velocity variation of the plane (z = 0.15 m) at the middle of the test section; the dimension of the contour is 0.55 m; the overvelocity region refers to the higher velocity region over the other region.

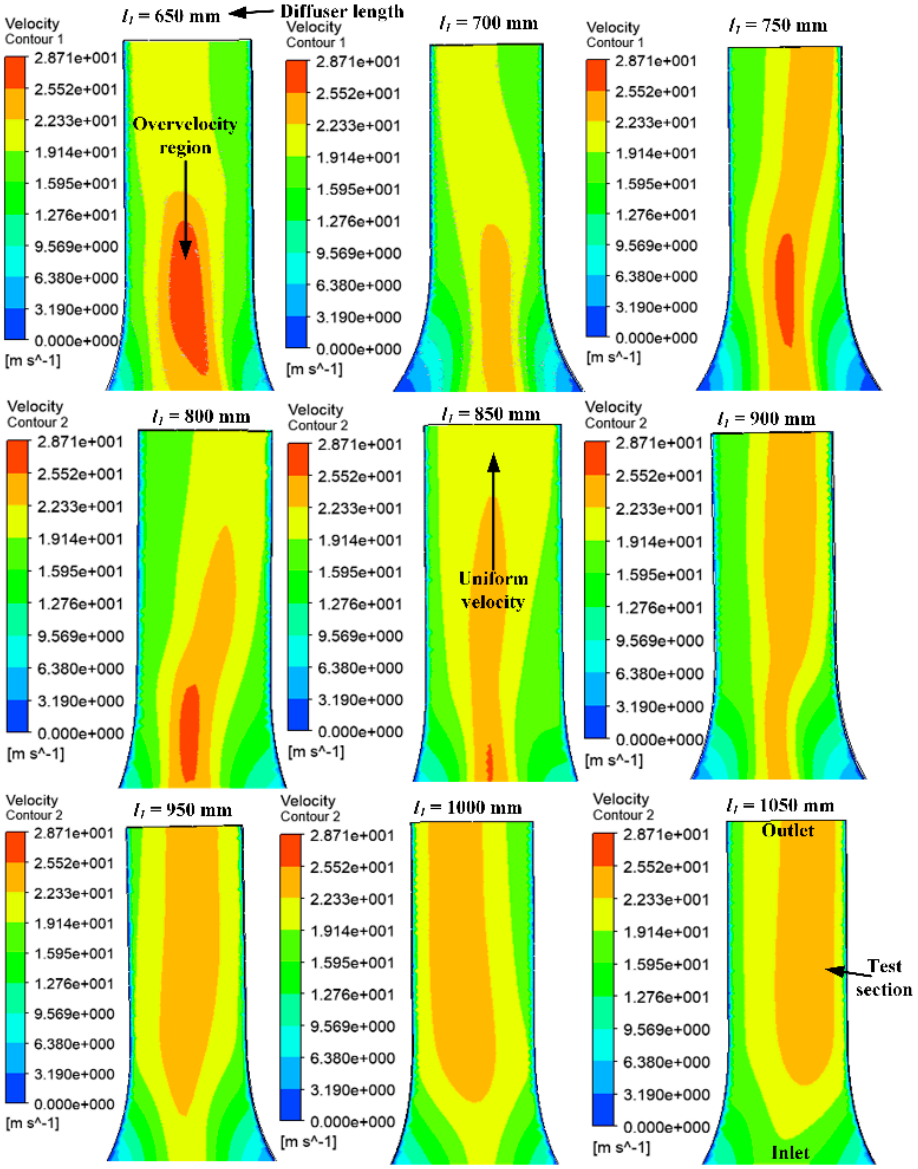

Figure 4. Velocity contour at various diffuser lengths.

As can be seen from Figure 4, the wind velocity distribution presents a gradient distribution from the center to the side walls. With the increase of the diffuser length, the entire plane wind velocity distribution uniformity also increases correspondingly. When the length of the diffuser section is 850 mm, the velocity distribution in most areas is relatively uniform. The velocity gradient is distributed symmetrically on both sides. Moreover, the uniform distribution of the wind velocity at the test section increases with the increase of the length of the diffuser, but the area with the higher wind velocity also

increases. Therefore, to weight the miniaturization of the wind tunnel and the uniformity of the flow field at the test section, a diffuser length of 850 mm was selected in this paper.

3.2. Influence of Contraction Length on Flow Field Uniformity

The longer length of the contraction section leads to an increase of the thickening of the boundary layer at the outlet and of the overall length of the wind tunnel. To obtain the appropriate length, the influence of the contraction length on the flow field characteristic at the test section was fully investigated. Figure 5 illustrates the variation of wind velocity distribution with axial distance under different contraction lengths.

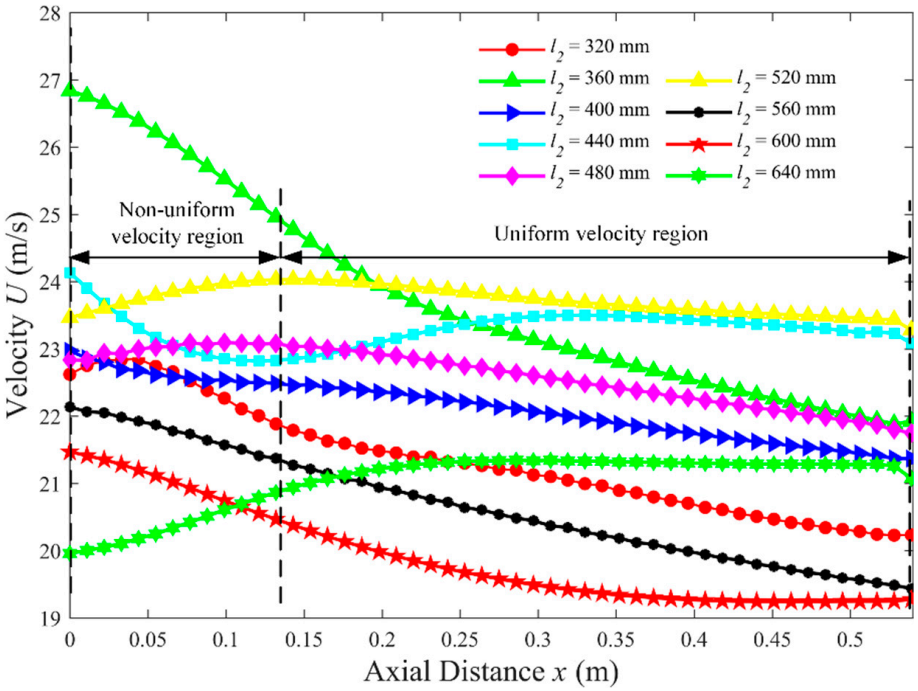

Figure 5. Variation of wind velocity distribution with axial distance under different contraction lengths.

Figure 5 demonstrates that the wind velocity tends to average 0.15 m after entering the test section for lengths of 600 mm and 640 mm. The longer contraction length can achieve a better uniform performance compared with the shorter length. It means that the wind tunnel can obtain a uniform flow field at the testing section. Therefore, it is suggested to adopt the longer contraction length when designing the wind tunnel.

To clearly demonstrate the influence of contraction lengths on the flow field characteristic, Figure 6 illustrates the velocity contour of the test section at various contraction lengths.

Figure 6 demonstrates that the wind velocity presents a gradient distribution from the center to the side walls. When the contraction length is shorter than 480 mm, an increase of the contraction length results in increasing the average distribution of wind velocity and decreasing the high velocity region to some extent. However, when the contraction length is higher than 480 mm, the distribution of wind velocity at the test section gradually leans to one side and presents an asymmetric distribution. That is because single-inlet blowers are found to produce a vortex-type flow (due to the asymmetric positioning of the impeller), which could aid wall flow attachment in the wide-angle diffuser. Moreover, the contraction length of 480 mm was selected in this paper to achieve better flow field characteristics.

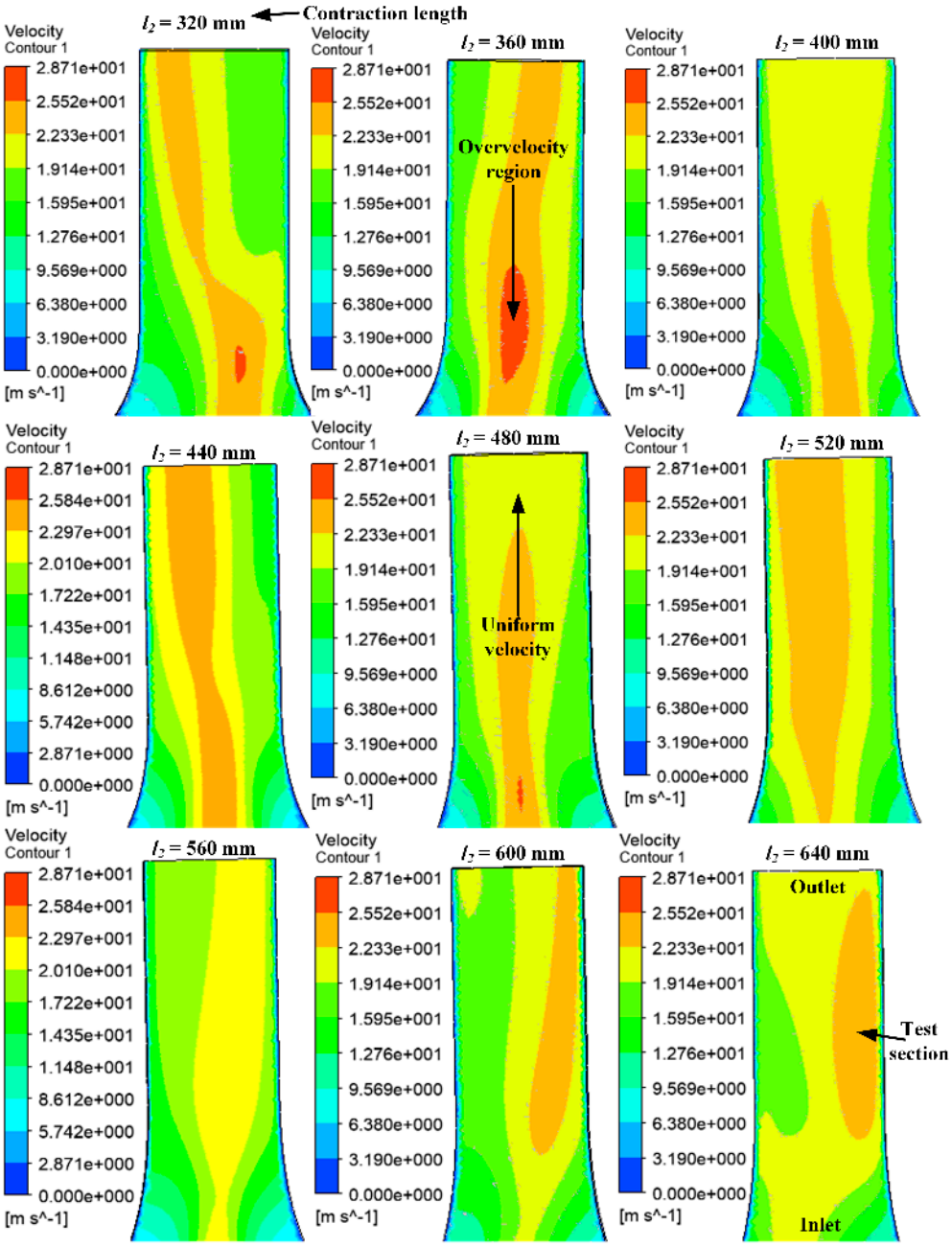

Figure 6. Velocity contour at various contraction lengths.

3.3. Influence of Honeycomb Porosity on Flow Field Uniformity

In order to improve the quality of the flow field at the test section of the wind tunnel, it is necessary to install a honeycomb, screens, and other porous plates at the rectification section. The honeycomb and screens that are installed at the rectification section can divide the large vortex within the airflow and attenuate its velocity component in the radial direction of the wind tunnel, so as to reduce the turbulence and stabilize the airflow. The honeycomb can also increase the contact area between the airflow and the wall, and the friction between the airflow and the wall is also conducive to reducing the turbulence of the airflow. The screen aims to produce a pressure drop on the airflow, which is beneficial to reduce the uneven axial velocity and the axial turbulence, and thus reduce the velocity fluctuation at the test section. Therefore, it is necessary to investigate the influence of the structural parameters of the honeycomb on the flow field.

When the airflow passes through the porous material, the viscous and inertia resistances are affected. In order to study the rectifying effect of different honeycomb parameters, the viscosity and inertia loss of the flow field under different honeycomb parameters should be explored. Its relationship can be expressed as follows [32]:

$$\frac{\Delta P}{\Delta \delta} = -S = \frac{\mu}{\alpha} v + \frac{C_2}{2} \rho v^2 \tag{2}$$

where ΔP represents the pressure difference between the two ends of the porous material; $\Delta \delta$ is the thickness of porous material, as shown in Figure 7; S is the momentum; μ represents the viscosity; v is the velocity; ρ refers to the density of air; $1/\alpha$ is the viscous resistance coefficient; C_2 represents the inertial resistance coefficient.

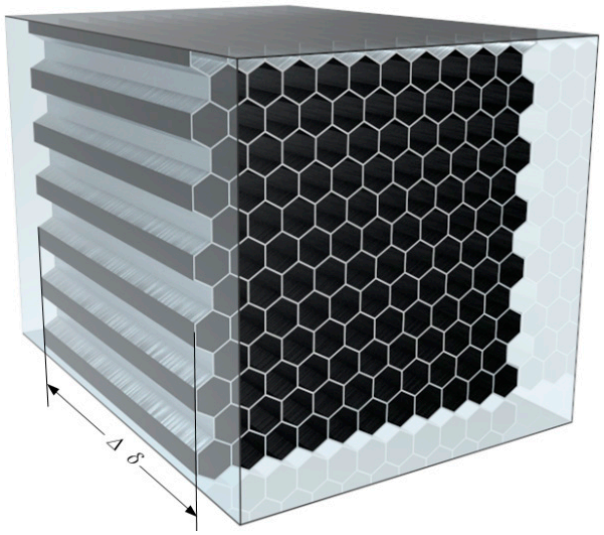

Figure 7. Finite element model of the honeycomb based on porous grid.

The viscous and inertial resistance coefficients of the porous material are related to the porosity, but not related to the thickness of the porous material. Therefore, to obtain the rectifying effect of different honeycomb parameters on the flow field, the finite element analyses model of the honeycomb flow field was established, as shown in Figure 7.

The pressure drop and flow field velocity on both sides of the honeycomb structure were obtained through the simulation analyses. Table 2 lists the viscous resistance coefficient $1/\alpha$ and the inertial resistance coefficient C_2. Therein, those parameters aim to simulate the honeycomb performance in the following analyses.

Table 2. Resistance coefficients.

Porosity	Velocity (m/s)	Pressure Drop (Pa)	Fitting Equation	Viscous	Inertial
0.9118	5	11.6659	$\frac{\Delta P}{\Delta \delta} = 4.091v^2 + 25.2388v$	0.0014	6.3426
	10	32.5798			
	15	65.1635			
	20	107.287			
	25	159.259			
0.8702	5	12.5922	$\frac{\Delta P}{\Delta \delta} = 4.7474v^2 + 27.2264v$	0.0015	7.3602
	10	36.8041			
	15	74.0126			
	20	122.629			
	25	182.02			

Table 2. *Cont.*

Porosity	Velocity (m/s)	Pressure Drop (Pa)	Fitting Equation	Viscous	Inertial
0.8339	5	13.8446	$\frac{\Delta P}{\Delta \delta} = 5.9966v^2 + 25.437v$	0.0014	9.2971
	10	41.9094			
	15	86.5913			
	20	145.894			
	25	218.701			
0.8004	5	15.5627	$\frac{\Delta P}{\Delta \delta} = 7.0467v^2 + 27.8077v$	0.0015	10.9252
	10	48.1755			
	15	100.464			
	20	169.51			
	25	254.356			
0.7666	5	17.4075	$\frac{\Delta P}{\Delta \delta} = 8.4313v^2 + 31.1299v$	0.0017	13.0717
	10	56.163			
	15	118.335			
	20	200.297			
	25	301.177			

The rectifying effect of the honeycomb mainly depends on its porosity, and the porosity does not affect the honeycomb shape [33]. Therefore, it is required to investigate the influence of the honeycomb porosity on the field uniformity. Figure 8 illustrates the variation of axial velocity distribution with axial distance at different honeycomb porosities.

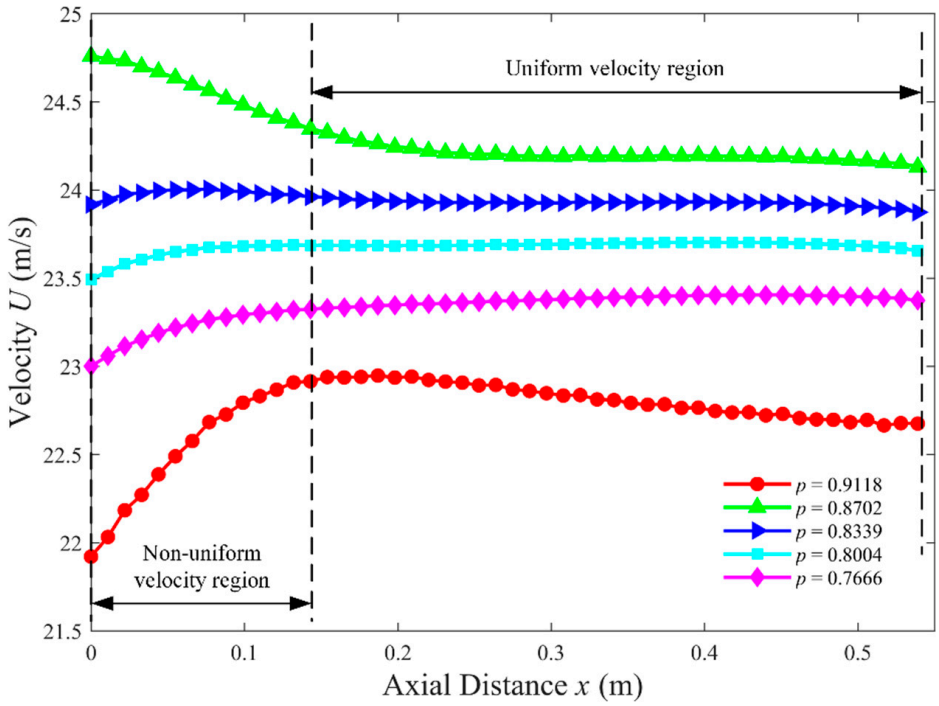

Figure 8. Variation of velocity distribution characteristics of the test section with axial distance under different honeycomb porosities.

As can be seen from Figure 8, the incoming airflow gradually tends to average after entering the test section between 0.1 m and 0.15 m. Axial wind velocity distribution along the center line of the test section is the most average when the porosity is 0.8339. Therefore, a porosity of 0.8339 was selected to achieve better flow field characteristics.

To clearly demonstrate the effect of the porosity on the flow field characteristics, Figure 9 illustrates the velocity and turbulence intensity contour of the test section under different porosities.

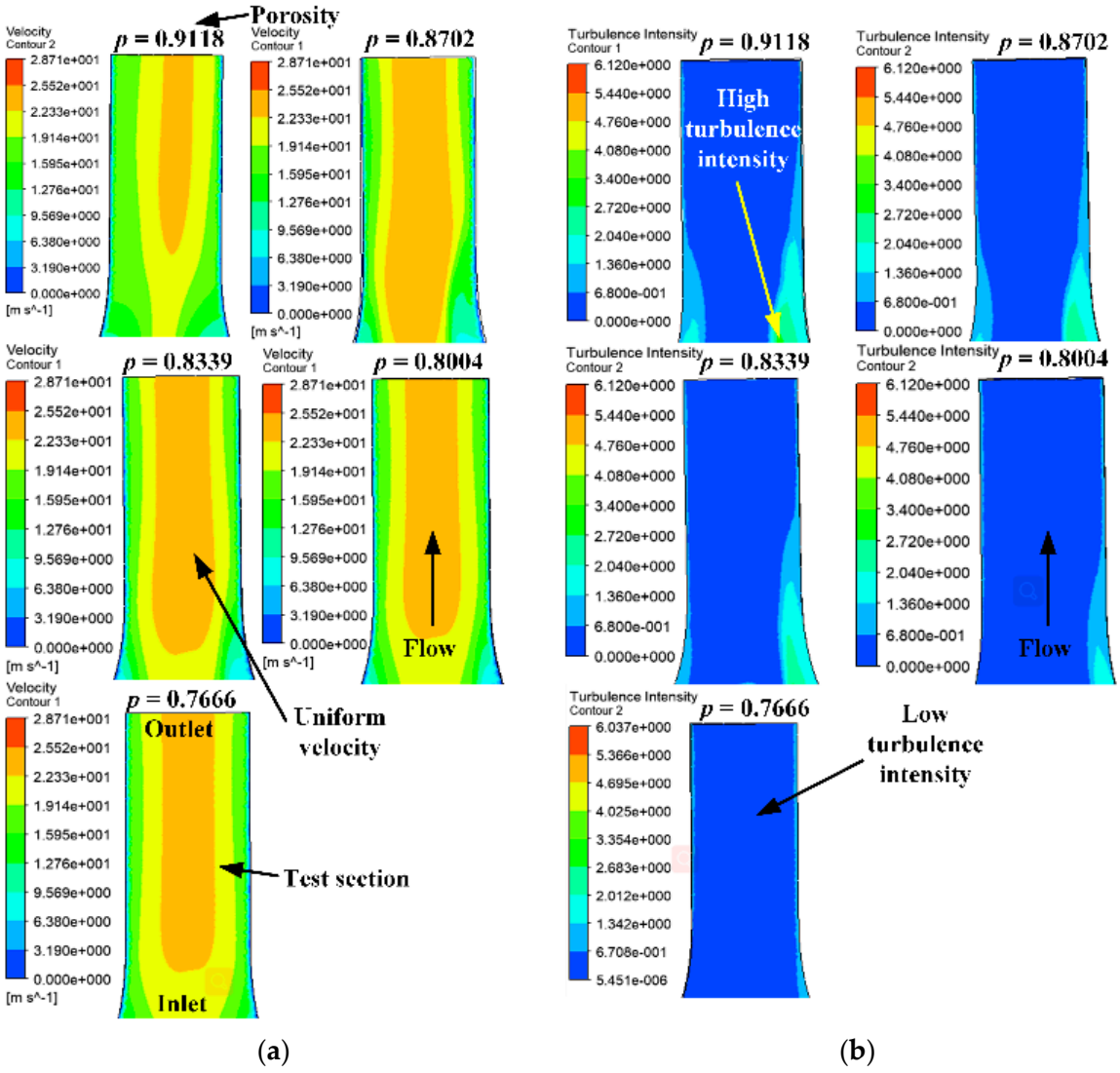

Figure 9. Velocity contour (**a**) and the turbulence intensity contour (**b**) at different honeycomb porosities.

Figure 9a shows a symmetrical gradient distribution of velocity at the test section, and the wind velocity distribution at the test section gradually becomes uniform with the decrease of the porosity. As can be seen from Figure 9b, most of the turbulence regions at the central line of the test section are relatively small. However, some higher turbulence regions also exist near the boundary. When the porosity of the honeycomb is decreased, the turbulence intensity of the test section correspondingly reduces. When the porosity is 0.7666, the turbulence intensity of the whole region is relatively average and within a relatively small range. Considering the uniformity of wind velocity distribution and the overall turbulence intensity, a honeycomb porosity of 0.8339 was selected in designing the wind tunnel.

3.4. Influence of Honeycomb Thickness on Flow Field Uniformity

The thicker the honeycomb is, the better the segmentation and straightening effect of the honeycomb can be obtained. However, a thicker honeycomb could cause a greater friction loss when the airflow passes through the wind tunnel. Therefore, in order to obtain

the appropriate honeycomb thickness, the flow field parameters of the test section under different honeycomb thicknesses were studied. Figure 10 illustrates the variation of axial wind velocity distribution with axial distance under different honeycomb thicknesses.

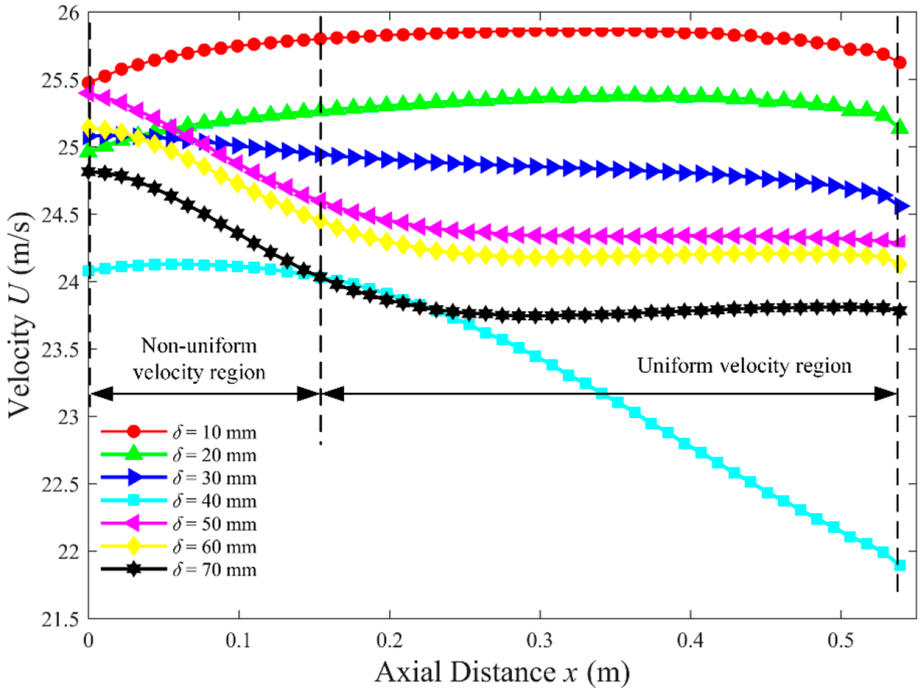

Figure 10. Variation of velocity distribution characteristics with axial distance under different honeycomb thicknesses.

It can be seen from Figure 10 that the wind velocity at the test section begins to be uniform from 0.1 to 0.15 m for most of the honeycomb thicknesses. When the honeycomb thickness is 30 mm, the velocity distribution on the axis of the wind velocity is the most uniform. Therefore, it is suggested to adopt a honeycomb thickness of 30 mm when designing the wind tunnel system.

The flow field contour is presented to clearly demonstrate the effect of the honeycomb thickness. Figure 11 illustrates the velocity and turbulence intensity contour at different honeycomb thicknesses.

Figure 11a demonstrates that when the honeycomb thickness increases from 10 mm to 20 mm, the velocity distribution tends to be uniform. However, with further increases of the honeycomb thickness, the velocity distribution becomes uneven. The honeycomb thickness of 20 mm is relatively uniform, and the wind velocity presents a symmetrical gradient distribution from the middle to both sides. The wind velocity distribution is most uneven when the honeycomb thickness is 40 mm, and the wind velocity is distributed to one side. It is worth pointing out that the boundary layer at the test section tends to thicken with the increase of the thickness of the honeycomb. Figure 11b shows that the turbulence intensity at the test section first increases and then decreases with the increase of the thickening of the honeycomb, and the larger turbulence intensity area is distributed to one side. When the honeycomb thickness is equal to 10 mm, the overall turbulence intensity at the test section is relatively small, and only the boundary layer has a certain turbulence intensity. The region with a higher turbulence is the largest at a honeycomb thickness of 40 mm. Note that the boundary layer increases with the increase of the honeycomb thickness. Because of the most average velocity distribution and relatively low turbulence intensity, a thickness of the honeycomb of 20 mm was selected for the current design.

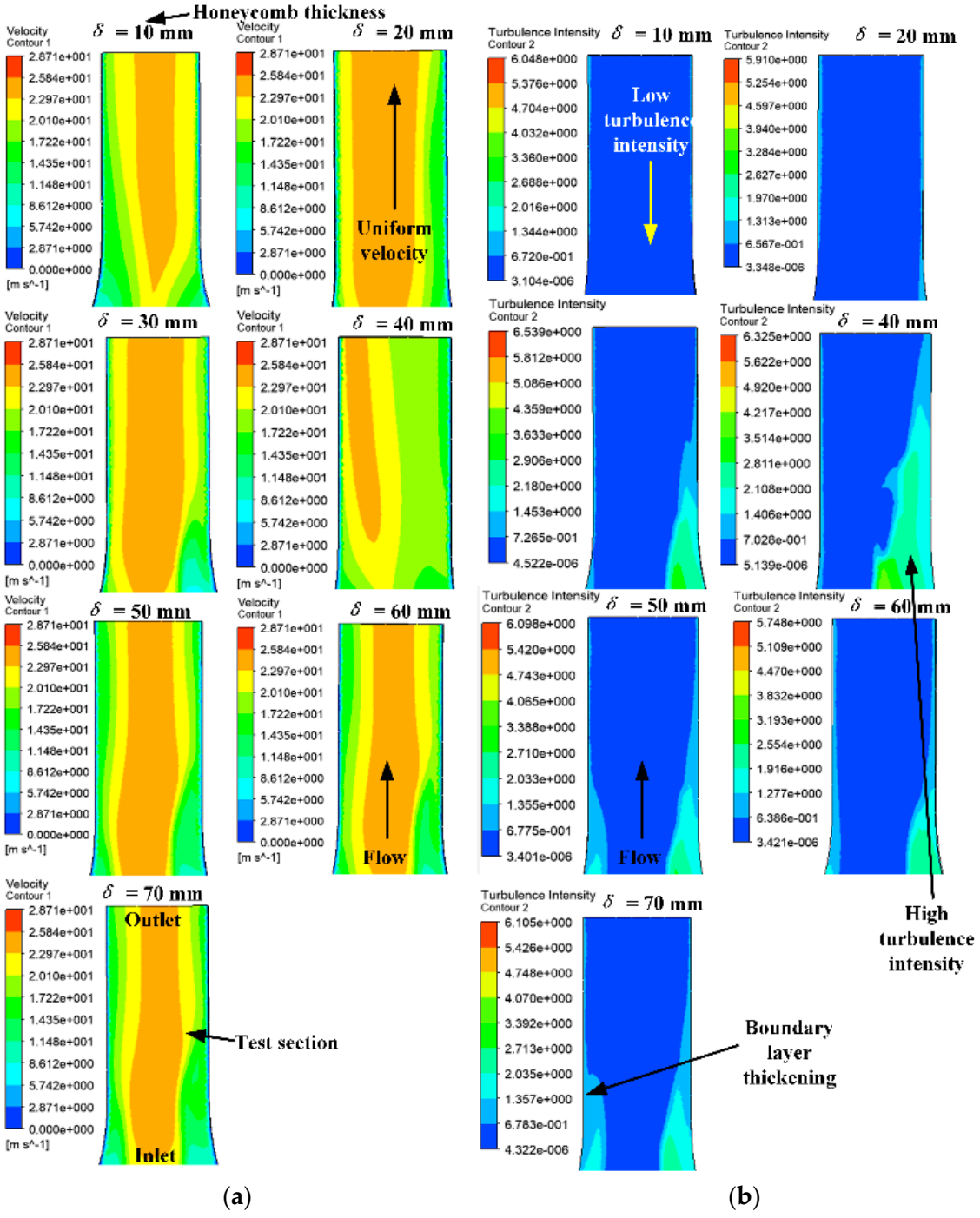

Figure 11. Velocity contour (**a**) and turbulence intensity contour (**b**) at various honeycomb thicknesses.

4. Experimental Validation and Discussion

Based on the above simulation analyses results, the optimal structural parameters were obtained, and a small and portable open-loop wind tunnel was built. In order to verify the simulation results, a prototype of the wind tunnel was fabricated, and the experimental analyses were carried out. Figure 12 illustrates the wind tunnel experimental system.

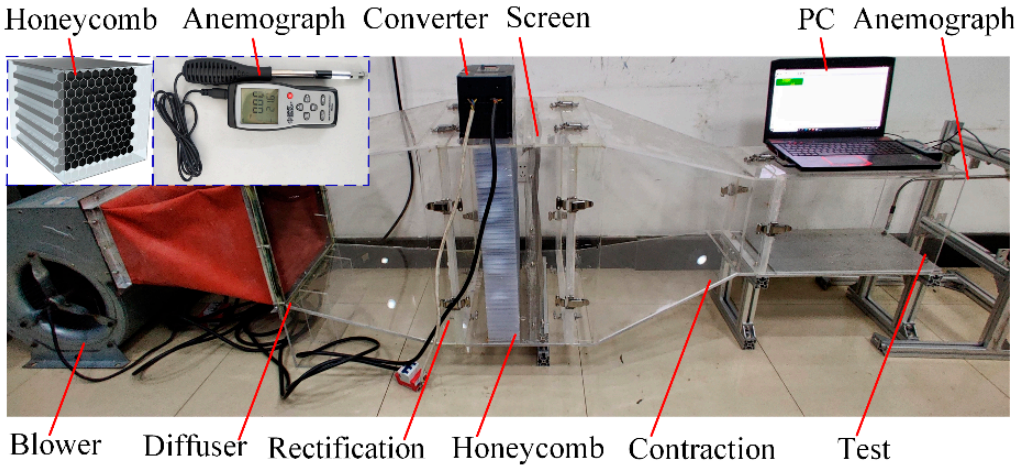

Figure 12. Wind tunnel experimental system.

The wind tunnel experimental system consists of the blower, wind tunnel, frequency converter, PC, and anemograph. Therein, the wind tunnel includes the diffuser, rectification, honeycomb, screen, contraction, and test section. The piezoelectric energy harvester is placed at the test section for capturing the aeroelastic vibration energy. The airflow velocity is measured by a thermal anemometer placed at the cross-section of the testing section.

To clearly demonstrate the performance of the designed wind tunnel, Figure 13 illustrates the variation of velocity with the converter frequency obtained experimentally and numerically. Therein, the airflow velocity is obtained by using the anemograph in the experiment and acquired by CFD in the simulation analyses; the fitted results refer to the experimental airflow velocity.

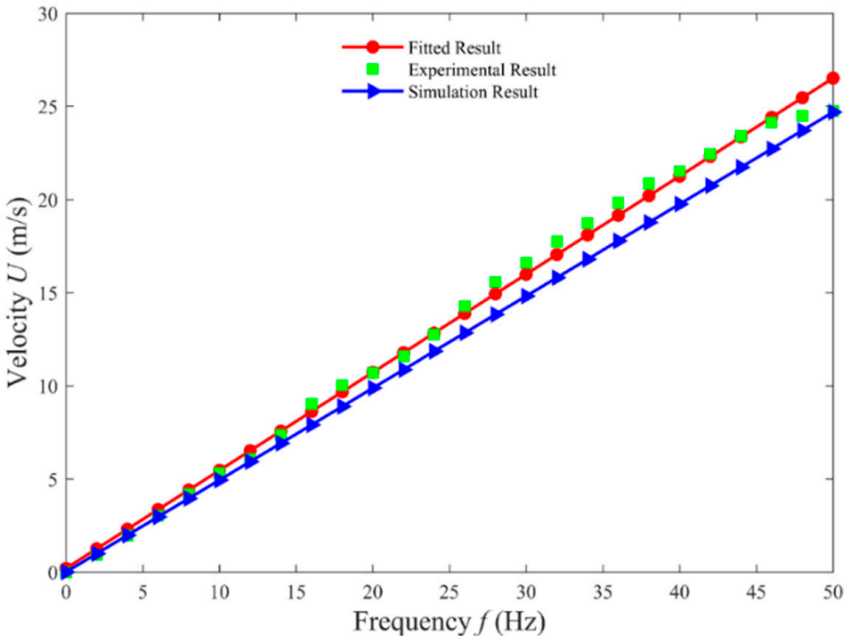

Figure 13. Variation of velocity with the converter frequency obtained experimentally and numerically.

As can be known from Figure 13 the experimental results are in good agreement with the simulation values, and the maximum difference is 9.5%. It is worth pointing out that the wind velocity changes linearly with the frequency, and the maximum wind velocity can reach 24.7375 m/s. The higher airflow velocity meets the requirement for wind energy harvesting at the designed wind tunnel.

To explicitly demonstrate the relation between the airflow velocity and frequency, the fitting equation was written as follows:

$$U = 0.5265f + 0.1939 \quad (3)$$

where, U represents the wind velocity at the outlet center of the test section; f is the frequency of the converter.

To demonstrate the uniform characteristic at the test section, Figure 14 illustrates the variation of velocity with the axial distance obtained experimentally and numerically.

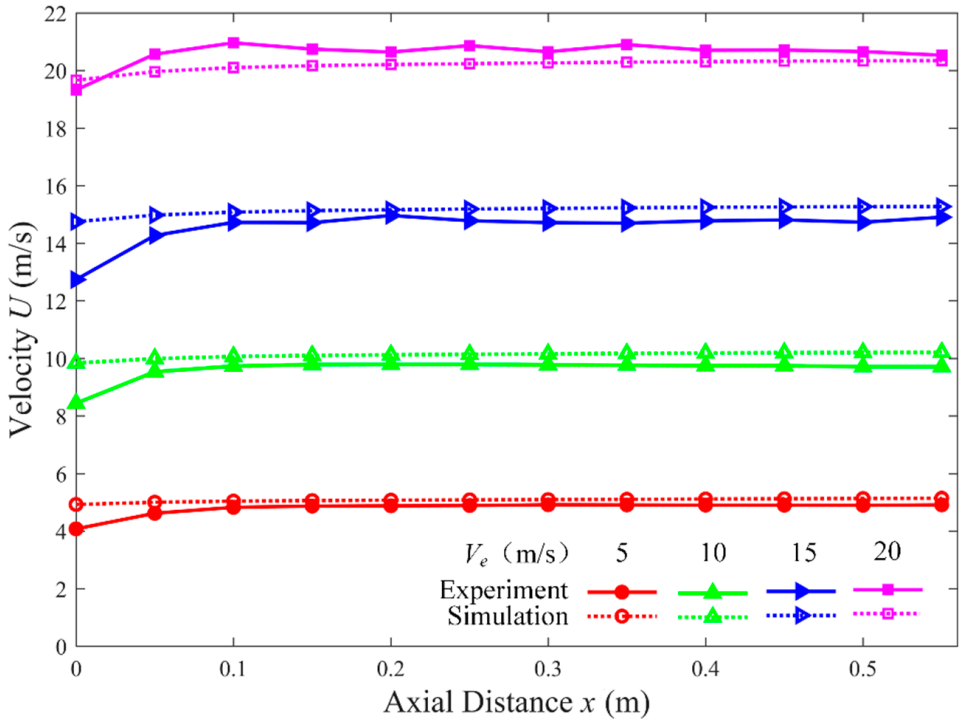

Figure 14. Variation of velocity with axial distance obtained experimentally and numerically.

It can be observed from Figure 14 that little difference exists in airflow velocity at the inlet of the test section. After entering the test section by 0.1 m, the flow velocity remains relatively stable and the fluctuation is small. Therefore, the simulation results are validated by the experiment, and the designed wind tunnel can achieve a stability and uniform airflow at the testing section.

It can be observed that the simulation results are consistent with the experimental results, and the error is within the acceptable range and the minimum error is only 1.23%. It means that the simulation analyses are both reasonable and effective, and the designed wind tunnel can obtain better performance. This wind tunnel was well utilized in exploring the designed energy harvester in [34].

Table 3 lists the relative error between the experimental results and the simulation values. Therein, the relative error (in percent) is obtained based on the experimental results.

Table 3. The relative errors (%) between the experimental and simulation results under various velocities.

Axial Distance (m)	Velocity (m/s)			
	5	**10**	**15**	**20**
0	19.67	16.57	15.93	4.26
0.05	8.99	5.73	5.80	1.90
0.10	4.92	3.79	2.80	3.85
0.15	4.06	3.27	2.87	2.77
0.20	3.85	3.21	1.23	2.26
0.25	3.65	3.21	2.43	3.37
0.30	3.13	3.37	2.86	2.31
0.35	3.25	3.50	2.98	3.54
0.40	3.37	3.66	2.45	2.57
0.45	3.42	3.65	2.24	2.61
0.50	3.50	3.98	2.77	2.34
0.55	3.20	4.00	1.61	1.72

5. Conclusions

This paper presented a small and portable open-loop wind tunnel for energy harvesting. The wind tunnel consisted of the diffuser, rectification, contraction and test section. The structure of the wind tunnel was first designed, the effects of the key structural parameters of the wind tunnel on the flow field characteristic were then investigated by using the simulation analyses, and the experimental prototype of the wind tunnel was finally fabricated to validate the numerical results. Results demonstrated that the distribution uniformity and average turbulence intensity of the airflow at the test section decreased first and then increased with the increase of the lengths of both the diffuser and contraction section, and also increased when decreasing the porosity and thickness of the honeycomb. When the diffuser and contraction lengths were 850 mm and 480 mm, respectively, and the porosity and thickness of the honeycomb were 0.8339 and 20 mm, respectively, a better distribution uniformity and a lower turbulence intensity can be obtained. The experimental results were in good agreement with the simulation values. The maximum wind velocity was up to 24.74 m/s, and the minimum relative error was only 1.23%. The designed wind tunnel can achieve the required wind velocity and meet the requirement of miniaturization. This work could provide an experimental foundation for investigating aeroelastic vibration energy harvesting.

Author Contributions: H.T.: conceptualization, validation, writing-original draft. T.H.: methodology, validation, resources. C.L.: data curation. H.C.: data curation, resources. X.S.: methodology, writing—review and editing, supervision, funding acquisition. All authors have read and agreed to the published version of the manuscript.

Funding: This work was financially supported by the National Natural Science Foundation of China (Grant No. 51875116).

Institutional Review Board Statement: Not applicable.

Informed Consent Statement: Not applicable.

Data Availability Statement: Not applicable.

Conflicts of Interest: The authors declare no conflict of interest.

References

1. Wang, Y.; Liu, D.; Xu, X.; Li, G. Investigation of reynolds number effects on aerodynamic characteristics of a transport aircraft. *Aerospace* **2021**, *8*, 177. [CrossRef]
2. Ocokoljić, G.; Rašuo, B.; Kozić, M. Supporting system interference on aerodynamic characteristics of an aircraft model in a low-speed wind tunnel. *Aerosp. Sci. Technol.* **2017**, *64*, 133–146. [CrossRef]
3. Beltramo, E.; Pérez Segura, M.E.; Roccia, B.A.; Valdez, M.F.; Verstraete, M.L.; Preidikman, S. Constructive aerodynamic interference in a network of weakly coupled flutter-based energy harvesters. *Aerospace* **2020**, *7*, 167. [CrossRef]
4. Xie, S.; Qu, J.; Han, Q.; Pang, Y. Wind dynamic environment and wind tunnel simulation experiment of bridge sand damage in xierong section of lhasa–linzhi railway. *Sustainability* **2020**, *12*, 5689. [CrossRef]
5. Wang, W.; Dun, H.; He, W.; Huang, N. Wind tunnel measurements of surface shear stress on an isolated dune downwind a bridge. *Appl. Sci.* **2020**, *10*, 4022. [CrossRef]
6. Lancelot, P.M.G.J.; Sodja, J.; Werter, N.P.M.; De Breuker, R. Design and testing of a low subsonic wind tunnel gust generator. *Adv. Aircr. Spacecr. Sci.* **2017**, *4*, 125–144. [CrossRef]
7. Capelli, L.; Sironi, S.; Del Rosso, R.; Centola, P. Design and validation of a wind tunnel system for odour sampling on liquid area sources. *Water Sci. Technol.* **2009**, *59*, 1611–1620. [CrossRef]
8. Cermak, J.E. Wind-tunnel development and trends in applications to civil engineering. *J. Wind Eng. Ind. Aerodyn.* **2003**, *91*, 355–370. [CrossRef]
9. Wittwer, A.R.; Möller, S.V. Characteristics of the low-speed wind tunnel of the unne. *J. Wind Eng. Ind. Aerodyn.* **2000**, *84*, 307–320. [CrossRef]
10. Abbaspour, M.; Shojaee, M.N. Innovative approach to design a new national low speed wind tunnel. *Int. J. Environ. Ence Technol.* **2009**, *6*, 23–34. [CrossRef]
11. Kalyulin, S.L.; Modorskii, V.Y.; Paduchev, A.P. Numerical design of the rectifying lattices in a small-sized wind tunnel. *AIP Conf. Proc.* **2016**, *1770*, 030110.
12. Şahin, B.; Ward-Smith, A.J. The pressure drop and flow characteristics of wide-angle screened diffusers of large area ratio. *J. Wind Eng. Ind. Aerodyn.* **1995**, *58*, 33–50. [CrossRef]
13. Fang, F.M.; Chen, J.C.; Hong, Y.T. Experimental and analytical evaluation of flow in a square-to-square wind tunnel contraction. *J. Wind Eng. Ind. Aerodyn.* **2001**, *89*, 247–262. [CrossRef]
14. Mehta, R.D.; Bradshaw, P. Design rules for small low speed wind tunnels. *Aeronaut. J.* **1983**, *83*, 443–453.
15. Ocokolji, G.; Damljanovi, D.; Vukovi, O.; Rauo, B. Contemporary frame of measurement and assessment of wind-tunnel flow quality in a low-speed facility. *FME Trans.* **2018**, *46*, 429–442. [CrossRef]
16. Rasuo, B. Scaling between wind tunnels-results accuracy in two-dimensional testing. *Trans. Jpn. Soc. Aeronaut. Space Sci.* **2012**, *55*, 109–115. [CrossRef]
17. Rasuo, B. The influence of reynolds and mach numbers on two-dimensional wind-tunnel testing: An experience. *Aeronaut. J.* **2011**, *115*, 249–254. [CrossRef]
18. Rasuo, B. On boundary layer control in two-dimensional transonic wind tunnel testing. In *IUTAM Symposium on One Hundred Years of Boundary Layer Research, Proceedings of the International Conference on Boundary and Interior Layers, Göttingen, Germany, 12–14 August 2006*; Springer: Berlin/Heidelberg, Germany, 2006; pp. 473–482.
19. Rahul, G.; Srijan, S.; Kumar, V. Design and simulation of a low speed wind tunnel with analysis of wind effects on an airfoil (cfd). In *Fluid Mechanics and Fluid Power—Contemporary Research*; Saha, A.K., Das, D., Srivastava, R., Panigrahi, P.K., Muralidhar, K., Eds.; Springer: New Delhi, India, 2017; pp. 539–549.
20. Moonen, P.; Blocken, B.; Carmeliet, J. Indicators for the evaluation of wind tunnel test section flow quality and application to a numerical closed-circuit wind tunnel. *J. Wind Eng. Ind. Aerodyn.* **2007**, *95*, 1289–1314. [CrossRef]
21. Gartmann, A.; Fister, W.; Schwanghart, W.; Muller, M.D. Cfd modelling and validation of measured wind field data in a portable wind tunnel. *Aeolian Res.* **2011**, *3*, 315–325. [CrossRef]
22. Quan, C.; Qian, K.; Asundi, A.; Chau, F.S.; Zhao, H.-Y.; Zhang, P.-F.; Ma, Y.; Ning, J.-G. The design of a low-speed wind tunnel for studying the flow field of insects' flight. In Proceedings of the International Conference on Experimental Mechanics, Singapore, 15–17 November 2014.
23. Mayer, Y.D.; Jawahar, H.K.; Szoke, M.; Ali, S.A.S.; Azarpeyvand, M. Design and performance of an aeroacoustic wind tunnel facility at the university of bristol. *Appl. Acoust.* **2019**, *155*, 358–370. [CrossRef]
24. Liu, P.Q.; Xing, Y.; Guo, H.; Li, L. Design and performance of a small-scale aeroacoustic wind tunnel. *Appl. Acoust.* **2017**, *116*, 65–69. [CrossRef]
25. Szőke, M.; Fiscaletti, D.; Azarpeyvand, M. Effect of inclined transverse jets on trailing-edge noise generation. *Phys. Fluids* **2018**, *30*, 085110. [CrossRef]
26. Showkat Ali, S.A.; Azarpeyvand, M.; Ilário da Silva, C.R. Trailing-edge flow and noise control using porous treatments. *J. Fluid Mech.* **2018**, *850*, 83–119. [CrossRef]
27. Arnold, B.; Lutz, T.; Krämer, E.; Rautmann, C. Wind-turbine trailing-edge noise reduction by means of boundary-layer suction. *AIAA J.* **2018**, *56*, 1843–1854. [CrossRef]
28. Avallone, F.; van der Velden, W.C.P.; Ragni, D. Benefits of curved serrations on broadband trailing-edge noise reduction. *J. Sound Vib.* **2017**, *400*, 167–177. [CrossRef]

29. Calautit, J.K.; Chaudhry, H.N.; Hughes, B.R.; Sim, L.F. A validated design methodology for a closed-loop subsonic wind tunnel. *J. Wind Eng. Ind. Aerodyn.* **2014**, *125*, 180–194. [CrossRef]
30. Leifsson, L.; Koziel, S. Simulation-driven design of low-speed wind tunnel contraction. *J. Comput. Sci.* **2015**, *7*, 1–12. [CrossRef]
31. Doolan, C.J. Numerical evaluation of contemporary low-speed wind tunnel contraction designs. *J. Fluid Eng.* **2007**, *129*, 1241–1244. [CrossRef]
32. Grumet, A.; Welder, W.; Peavey, C.; Grumet, A.; Welder, W.; Peavey, C. Navier-stokes analysis of nwtc back leg diffuser. In Proceedings of the 35th Aerospace Sciences Meeting and Exhibit, Reno, NV, USA, 6–9 January 1997.
33. Kulkarni, V.; Sahoo, N.; Chavan, S.D. Simulation of honeycomb–screen combinations for turbulence management in a subsonic wind tunnel. *J. Wind Eng. Ind. Aerodyn.* **2011**, *99*, 37–45. [CrossRef]
34. Shan, X.; Tian, H.; Cao, H.; Xie, T. Enhancing performance of a piezoelectric energy harvester system for concurrent flutter and vortex-induced vibration. *Energies* **2020**, *13*, 3101. [CrossRef]